Journal Pre-proofs

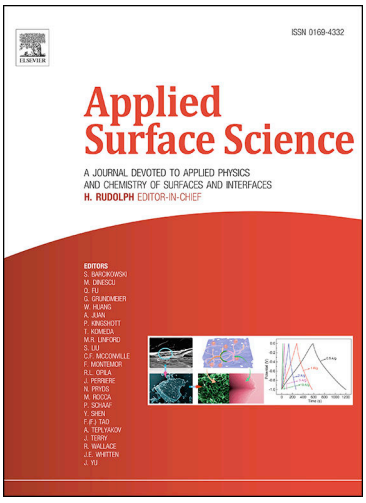

Porous Hierarchical TiO_2/MoS_2/RGO nanoflowers as Anode Material for Sodium Ion Batteries with High Capacity and Stability

Jingyun Ma, Mengdi Xing, Longwei Yin, Kwan San Hui, Kwun Nam Hui

PII: S0169-4332(20)32492-2
DOI: https://doi.org/10.1016/j.apsusc.2020.147735
Reference: APSUSC 147735

To appear in: *Applied Surface Science*

Received Date: 5 June 2020
Revised Date: 26 August 2020
Accepted Date: 28 August 2020

Please cite this article as: J. Ma, M. Xing, L. Yin, K. San Hui, K. Nam Hui, Porous Hierarchical TiO_2/MoS_2/RGO nanoflowers as Anode Material for Sodium Ion Batteries with High Capacity and Stability, *Applied Surface Science* (2020), doi: https://doi.org/10.1016/j.apsusc.2020.147735

Porous Hierarchical TiO_2/MoS_2/RGO nanoflowers as Anode Material for Sodium Ion Batteries with High Capacity and Stability

Jingyun Ma*[a], Mengdi Xing[a], Longwei Yin*[b] Kwan San Hui*[c], Kwun Nam Hui [d]

[a]School of Materials Science and Engineering, Qilu University of Technology (Shandong Academy of Science), Jinan 250353, P. R. China School of Materials Science and Engineering, Qilu University of Technology (Shandong Academy of Science)

[b]Key Laboratory for Liquid-Solid Structural Evolution and Processing of Materials, Ministry of Education, School of Materials Science and Engineering, Shandong University, Jinan 250061, P. R. China

[c]Engineering Faculty of Science, University of East Anglia, Norwich, NR4 7TJ, United Kingdom

[d]Institute of Applied Physics and Materials Engineering, University of Macau, Avenida da Universidade, Taipa, Macau, China

*To whom correspondence should be addressed. Tel.: + 86 531 89631227. Fax: + 86 531 89631227. E-mail: mjy2003@qlu.edu.cn, yinlw@sdu.edu.cn.

Abstract To enhance the reversible capacity and cycle stability of MoS_2 as anode materials for sodium ion batteries (SIBs), we constructed a hybrid architecture composed of MoS_2 and TiO_2 nanosheets, linking with reduced graphene oxide (RGO) to another TiO_2/MoS_2 to form a nanoflower structure. Owing to layered RGO coupled with TiO_2/MoS_2 hybrid, such a composite offered interconnected conductive channels to short shuttle path of Na^+ ions and favorable transport kinetics under charge/discharge cycling. Moreover, this unique structure showed a porous and hierarchical architecture, which not only buffered volume changes but also provided more electrochemical active sites during insertion/deintercalation processes of Na ions. Outstanding electrochemical performances were identified by the component matching effect among TiO_2, MoS_2 and RGO with a three-dimensional (3D) interconnected network, exhibiting a good reversible capacity of 616 mA h g^{-1} after 100 cycles at 0.1 A g^{-1}, an excellent rate capability of 250 mA h g^{-1} even at 5A g^{-1} and a long cycling stability of 460 mA h g^{-1} with a capacity fluctuation of 0.03% per cycle within 350 cycles at 1 A g^{-1}.

Keywords: Sodium ion batteries; interconnected network; TiO_2/MoS_2/RGO; component matching effect; cycling stability

1. Introduction

Nowadays, considering the low cost, natural abundance and environmental benignity, sodium (Na) presents as a promising alternative of the metal lithium (Li) in practical applications of energy storage devices.[1-5] However, compared to Li^+ (0.76 Å), the ionic radius of 1.06 Å for Na^+, it is found that exploring appropriate anode materials to hold sodium ions in sodium ion batteries (SIBs) is full of huge challenges.[6] To this regard, numbers of research works have been put into practice to explore

superior electrodes that can enhance their energy density. Such as hard carbon,[7] porous and hollow carbon hybrid with other composite materials,[8-10] titanium-based materials,[11] transitional metal dichalcogenides,[12,13] metal oxide[14], another alloying-type metallic Sn-Ge[15] and Sb[16] have been reported. Among them, there is an S-Mo-S three-atom layer in exfoliated MoS_2 possesses and the interlayer distance can reach 0.62 nm.[17] Inspired by this, many works have demonstrated that MoS_2 has the potential as anode electrode of SIBs.[18,19] Unfortunately, two-dimensional (2D) MoS_2 with layered structure is easy to stack, which is ascribed to its surface energy and Van de Waals attraction among interlayers. When used as an anode electrode for SIBs, the stacked layers are ready for fast capacity fading and poor rate ability under the condition of metal ion insertion/de-intercalation cycling process.[20] In order to solve the problem derived from shortcomings existing in electrochemical performance of MoS_2 electrodes, an effective strategy is to find suitable nanomaterials to prevent restacking of MoS_2 layers. Due to desirable physicochemical properties, such as nontoxicity, low cost and chemical stability, TiO_2 nanostructure has been identified to be a perfect backbone of MoS_2 through hybridization, acting as host for metal ions, such as TiO_2 nanowire@MoS_2 nanosheet,[21] TiO_2@MoS_2 microspheres,[22] and core-shell TiO_2@MoS_2 compositions.[23] However, the low electronic conductivity and sluggish lithium/sodium ions transport power of TiO_2 electrodes, resulting in a low power density.

In previous works, reduced graphene oxide (RGO) nanolayers are introduced in MoS_2-based electrode compositions, whose aim is to reduce the transfer distance of electrons and Na^+ ions as well as relieve the volume change. For example, when graphene sheets cover 3D MoS_2 micro-flowers, the MoS_2/graphene network composition will exhibit an outstanding specific capacity of 500 mA h g^{-1} at 100 mA g^{-1}, showing a remarkable rate performance of 345 mA h g^{-1} at 1600 mA g^{-1}.[24] Additionally, owning to the excellent structure compatibility of MoS_2 nanosheets with RGO nanosheets,[25] we

expected that the problem of stacking of TiO_2/MoS_2 could be addressed by forming a 3D TiO_2/MoS_2/RGO nanoflower structure based on Van der Waals interaction, which could promote the insertion/de-intercalation of sodium ions during repeated charge/discharge cycling.

In this work, we rationally designed and synthesized RGO-interconnected TiO_2/MoS_2 nanohybrids with a porous hierarchical structure to enhance the capacity and overall stability during the charge/discharge process of sodium ions battery. The porous hierarchical TiO_2/MoS_2/RGO nanohybrid had low electrons and ion transfer resistances, together with a good electrode integrity derived from the robust structural architecture. Compared to MoS_2 and TiO_2/MoS_2, TiO_2/MoS_2/RGO nanohybrids showed a high reversible capacity of 616 mA h g^{-1} at 0.1 A g^{-1} after 100 cycles and a stable long cycling life with a capacity fluctuation of only 0.03% per cycle within 350 cycles at 1.0 A g^{-1}. It revealed that TiO_2/MoS_2/RGO presented an ultrahigh structural integrity after going through 350 cycles. Furthermore, the synergistic effect among TiO_2, MoS_2 and RGO provided effective electron transfer and ion diffusion spaces, promoting insertion/deintercalation processes of Na ions.

2. Experimental Section

2.1 Materials synthesis

All chemical materials derived from analytical grade, which were purchased from China National Pharmaceutical.

2.1.1 Fabrication of TiO_2 nanosheets. In a typical synthesis process,[26] 2.4 ml hydrofluoric acid solution (40 wt%) was added in 20 ml titanium butoxide ($Ti(OC_4H_9)_4$). After ultrasonicating 30 minutes, a solution was transferred to a 100 ml kettle autoclave, then treated at 200 ^oC for 24 h. After cooling down to the room temperature, the TiO_2 precipitate was collected by washed 3 times with de-ionized water water and ethanol, respectively. Then dried at 60 ^oC for 12h. Finally, 1.0 g TiO_2 and 0.8 g urea were collected to grind with 5 ml H_2O, annealed at 500 ^oC for 2 h under air. The obtained

product is designated as TiO_2 nanosheets.

2.1.2 Fabrication of porous hierarchical structured TiO_2/MoS_2/RGO nanohybrids. Fig. 1 illustrates the fabrication procedure for porous hierarchical structured TiO_2/MoS_2/RGO nanohybrids. First, according to the reported literature,[27] the graphene oxide (GO) suspension with 2 mg/L was synthesized by the modified Hummer's method. Then 5ml GO solution was injected into 20 ml DI water with ultrasound operation for 2 h. Meanwhile, 75 mg TiO_2 nanosheets were poured into 60 ml DI water, a homogeneous cream yellow solution A can be got under stirring for 5 minutes. Then, 0.8 ml silane coupling agent was dropped into the solution A under ultrasonicating operation. Afterward, 20 ml GO suspension was added into above solution with drop by drop. After ultrasonication for 5 minutes, 0.35 g ammonium molybdate tetrahydrate and 0.76 g thiourea were gradually added to the solution under stirring for 30 minutes. Finally, the resultant solution was transferred into 100 ml Teflon-lined autoclave, then put into oven at 200 ^{o}C for 20 h. The resultant precipitants were washed with water and ethanol by filtration three times, respectively. After drying at 60 ^{o}C for 12 h, the as-prepared product was annealed at 500 ^{o}C for 2 h under Ar environment with a heating rate of 3 ^{o}C min^{-1}, which designated as TiO_2/MoS_2/RGO nanohybrids. As a comparison, similar processes for preparing MoS_2 and TiO_2/MoS_2 were carried out without the addition of TiO_2 and RGO, RGO, respectively.

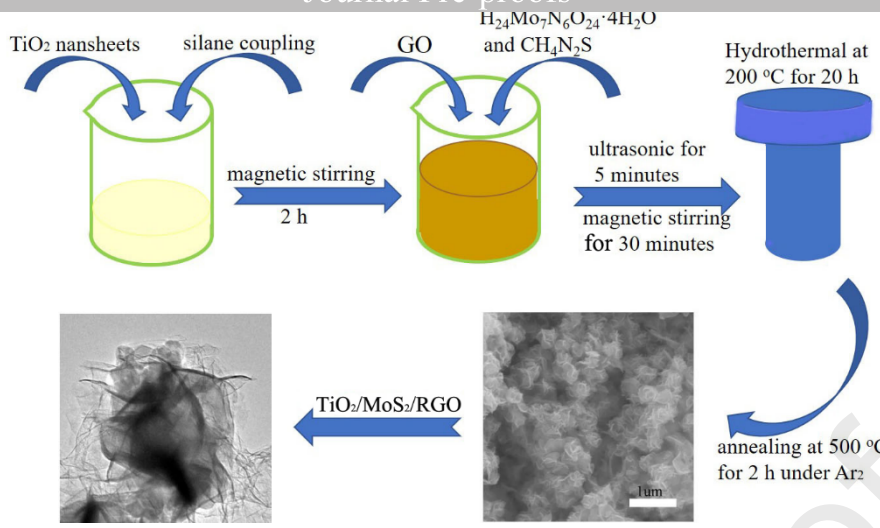

Fig. 1 Schematic diagram of the fabrication procedure for the TiO_2/MoS_2/RGO nanohybrids.

2.2 Material characterization.

Morphology of the samples were checked via a SU-70 field emission scanning electron microscopy (FE-SEM). Under an acceleration voltage of 200 kV, a high-resolution transmission electron microscopy (HR-TEM) with JEM-2100 (JEOL) was carried out to obtain morphology and structural information of the products. The crystal structural characterization of samples was measured via a Rigaku D/Max-Rb diffractometer armed with Cu Ka radiation (λ = 1.5406 Å). The X-ray photoelectron spectroscopy (XPS) could be probed with an ESCALAB 250 instrument using a 150W Al Ka probe beam. At 77 K, N_2 adsorption-desorption measurements were operated via a Gold APP V-Sorb 2800P. Brunauer-Emmett-Teller (BET) method and Barrette-Joynere-Halenda (BJH) method were used to calculate specific surface areas and porosity distributions. The Raman spectroscopy was analyzed via a Renishaw 2000 Raman microscope.

2.3 Electrochemical measurements.

Firstly, some slurry was made by the mixture with 70 wt% of produced materials, 15 wt% of LA132 binder and 15 wt% of acetylene carbon black. Then, the mixed slurry was evenly smoothed on a copper foil with a paper blade. The copper foil was heated to 60 °C to form an active working electrode. Then cut it into round geometrical shapes with a diameter of 12 mm. The weight of active

materials used for electrochemical study was about 1.0 mg cm^{-2}. Electrochemical tests were performed using 2025 coin-type cells, with the TiO_2/MoS_2/RGO acted as a working electrode and a sodium metal foil as a counter electrode, a glass fiber as a separator. 1.0 M of $NaClO_4$ in ethylene carbonate: propylene carbonate (1:1 by volume) with 5 wt% of fluoroethylene carbonates was used as the electrolyte. Fresh coin cells were assembled in an Ar-filled glove box. A discharge/charge performance assessment was performed through a LAND CT2001A battery test system from 3.0 V to 0.01 V under room temperature. Cyclic Voltammetry (CV) behaviors and electrochemical impedance spectroscopy measurements were respectively investigated in an electrochemical workstation (PARSTAT 2273) at a scan rate of 0.1 mV s^{-1} within a frequency range from 100 kHz 10 mHz for an amplitude of 5 mV.

3. Results and discussion

The crystalline phase component of the prepared samples was identified by XRD patterns. From Fig. 2a, at the 2θ degree of 25.3°, 37.8°, 48.0°, 53.9°, 55.1°, 62.7° and 68.8°, these sharp characteristic peaks were respectively pointed to crystalline planes at (101), (004), (200), (105), (211), (204), and (116) with a tetragonal structured anatase TiO_2 (JCPDS No. 21-1272)[28]. At 22-26°C, there was a broad and weak diffraction peak, which was corresponding to the graphite structure of RGO.[29,30] The diffraction peaks of 14.4°, 32.7°, 33.5° and 58.3° could be respectively traced to crystalline planes at (002), (100), (101) and (110) for hexagonal MoS_2 (JCPDS No. 37-1492)[31]. The quantitative phase and lattice parameters of composition component of TiO_2/MoS_2/RGO were evaluated via Rietveld refinement of XRD (Fig. S1 (Supplementary Information)). The results indicate that Rietveld parameters are: Rexp=3.89%; Rwp=4.20%; Rp=5.19% and GOF=1.08. Table S1 shows that the mass percent of MoS_2, TiO_2 and graphitization of RGO is 17.67%, 35.47% and 27.78%, respectively. For TiO_2 phase, the value of R-Bragg is 0.813; the lattice parameters are a=b/Å=3.892 and c/Å=9.464;

the average crystallite size is about 19.42 nm. Compared to previous works and commercial anatase TiO_2,[32-34] the TiO_2 phase shows a more open nanostructure with a and b of higher values, which is more liable to hybridize MoS_2 (17.67 wt%) with TiO_2 (35.47 wt%). Therefore, the existence of TiO_2 nanosheets promotes the formation of TiO_2/MoS_2.

The Raman spectra confirms the existence of RGO. This view has been explained by the two peaks of 1361 and 1585 cm^{-1}, corresponding to the band D and band G of RGO[35]. After RGO was combined with TiO_2/MoS_2, the broadened peaks of TiO_2/MoS_2/RGO nanohybrids showed the disordered stacking nature of RGO sheets, as is shown in Fig. 2b. For the purpose of contrast, MoS_2 and TiO_2/MoS_2 were prepared by similar hydrothermal method. Fig. S2 shows the powder XRD patterns of crystal compositions of TiO_2, MoS_2 and TiO_2/MoS_2. All diffraction peaks of the samples can be labelled by cards of JCPDS No. 21-1272 and JCPDS No. 37-1492.

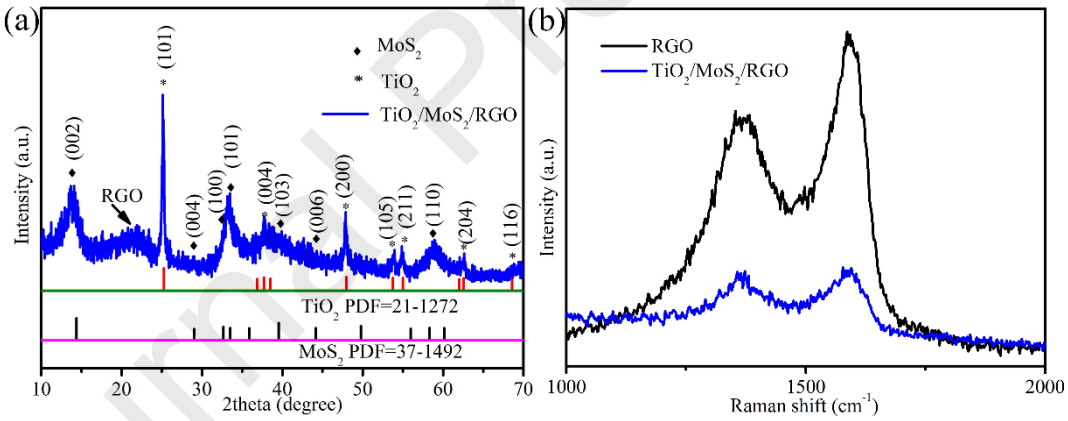

Fig. 2 (a) XRD patterns of TiO_2/MoS_2/RGO and the standard patterns of TiO_2 and MoS_2, (b) Raman spectrum of pure RGO and TiO_2/MoS_2/RGO.

To probe chemical components and chemical element binding energies of the samples, an X-ray photoelectron spectroscopy (XPS) test was carried out to get specific data. In Fig. S3, Mo, S, Ti, O and C are clearly displayed in the XPS survey spectrum for TiO_2/MoS_2/RGO powders. The detected atomic percent of Ti, Mo, S, C and O was 1.08%, 12.72%, 22.42%, 46.14% and 17.63%, respectively. The high oxygen content is attributed to the fact that the sample was exposed to air for a long time.

In Fig. 3a, two peaks located at around 458.8 and 464.8 eV, ascribed to Ti $2p_{3/2}$ and Ti $2p_{1/2}$ respectively. Compared to bare TiO_2 and some other TiO_2 compounds[36,37], the difference value of binding energy ΔE between Ti $2p_{3/2}$ and Ti $2p_{1/2}$ is about 6 eV, confirming the oxidation state of Ti (Ⅳ). As is shown in Fig. 3b, three prominent peaks with binding energies of 229.6, 232.8 and 235.4 eV, corresponding to oxidation sate with $Mo^{4+}3d_{5/2}$, $Mo^{4+}3d_{3/2}$ and $Mo^{6+}3d_{3/2}$ 2p.[38,39] The results suggest that there is a small number of MoO_2 and molybdate in the TiO_2/MoS_2/RGO compound owing to surface oxidation. From Fig. 3c, binding energies of 161.8 eV and 163.0 e V can be referred to as peak $S^{2-}2p_{3/2}$ and peak $S^{2-}2p_{1/2}$.[40] Furthermore, after devolution of C1s spectra, three peaks are observed at 284.8, 286.0 eV and 288.4 eV (in Fig. 3d), assigned to C-C, C-O and O=C-O bonds respectively. In the reported work[41,42], there are similar results for C 1s spectrum of RGO, as binding energies of sp^2 C-C and C-O bonds are located at 284.6 and 286.7 eV.

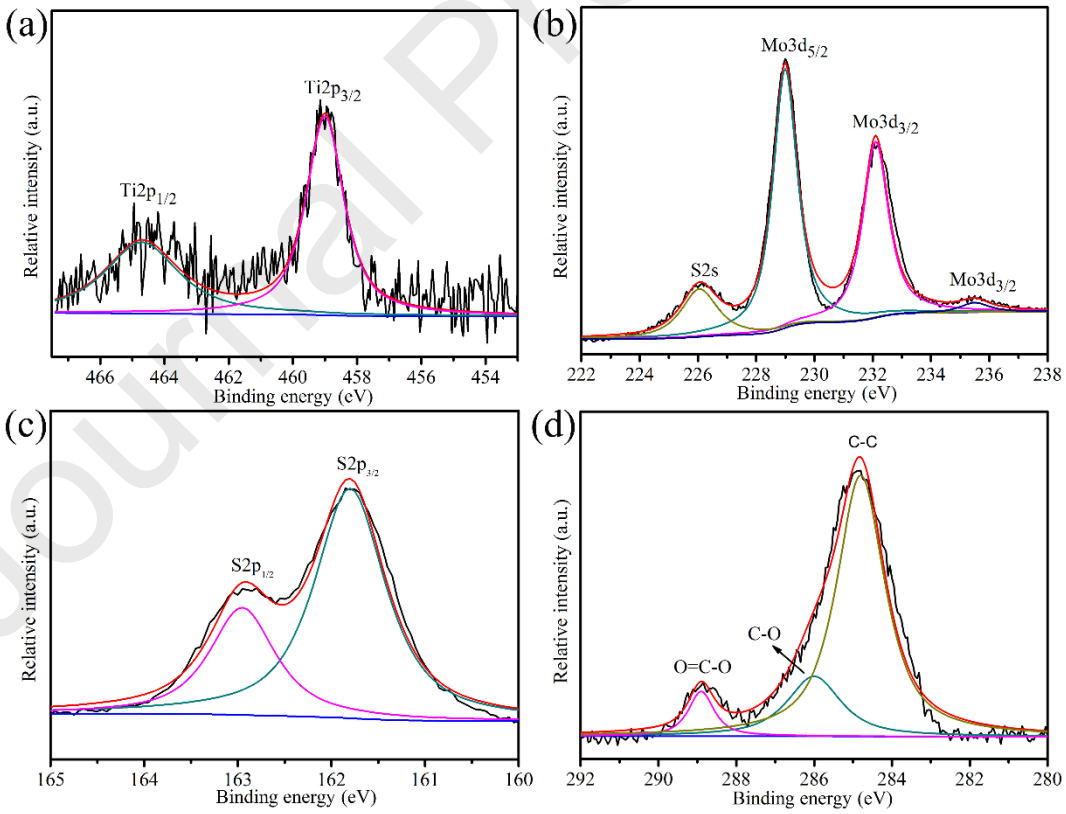

Fig. 3 The high resolution X-ray photoelectron spectroscopy (XPS) of TiO_2/MoS_2/RGO. (a) Ti 2p, (b) Mo 3d, (3) S 2p, (4) C 1s.

In order to detective morphology profiles and microstructures of the samples, a scanning electron microscopy (SEM), a transmission electron microscopy (TEM) and corresponding element mapping images were taken as observation media. As is shows in Fig. S4a, the TiO_2 nanosheets present a regular rectangle shape with an average lateral size of 30-40 nm. After integrating MoS_2 with TiO_2 nanosheets, TiO_2/MoS_2 composites (Fig. S4b) presented flower microspheres with a three-dimensional architecture, which was generated from the high surface energy and interlayer Van der Waals attraction of MoS_2 (Fig. S4c). After combining with RGO, chiffon-like RGO nanosheets with crinkled textures were tightly wrapped on the surface of TiO_2/MoS_2 flower, forming a TiO_2/MoS_2/RGO porous hierarchical hybrid nanostructure (See Fig. 4a). Fig. 4b shows that the chiffon-like RGO plays the role of a bridge, interconnecting TiO_2/MoS_2 flowers. In Fig. 4c, the selected area electron diffraction (SAED) image for TiO_2/MoS_2/RGO sample, presents clear diffraction rings, which can be well indexed as a pure hexagonal MoS_2 and anatase TiO_2 phase, indicating the polycrystalline feature of the composite. The diffraction rings are well matched with plane (101) and (103) of MoS_2 as well as plane (101) and (211) of anatase TiO_2, further confirming the presence of MoS_2 and TiO_2. From Fig. 4d, the lattice fringes of TiO_2 and MoS_2 are found in the HRTEM image. The marked d-spacing of 0.35 nm is relates to interplane spacing (101) of TiO_2, while 0.62 nm can be assigned to crystalline planes (002) of MoS_2.

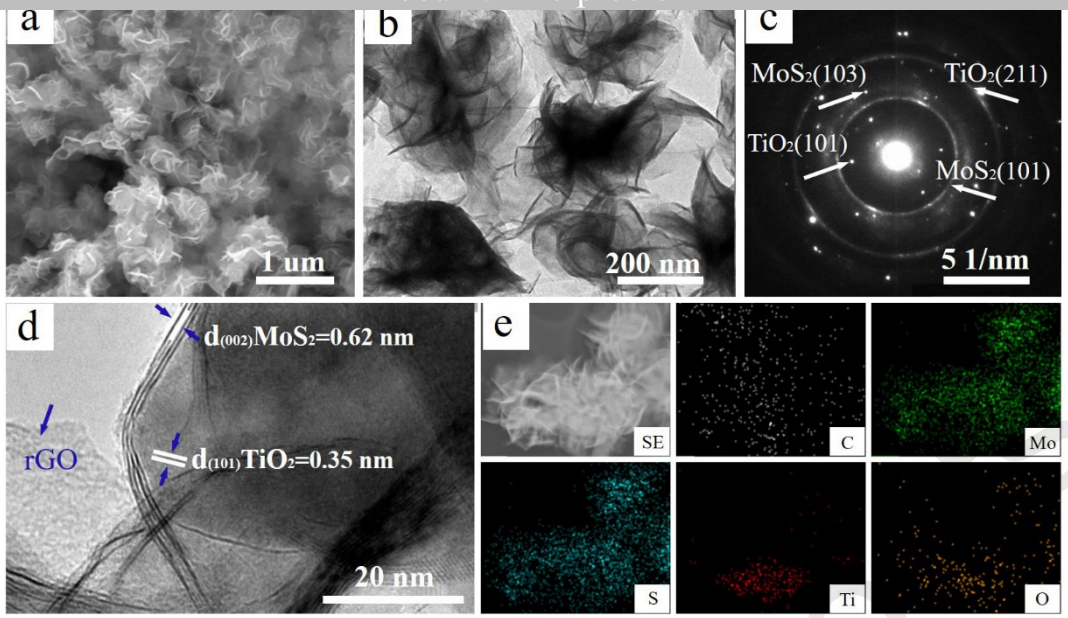

Fig. 4 Morphological characterization of TiO_2/MoS_2/RGO nanohybrid. (a) SEM images, (b) TEM images, (c)SAED pattern (d) HRTEM lattice image and (e) TEM image and elements mappings.

The detailed microstructures of the TiO_2/MoS_2/RGO sample were investigated by typical EDS mapping. Fig. 4e demonstrates that Mo, Ti, S, and C elements are clearly distributed on the micro-flowers. It is also revealing that multilayers MoS_2 hybrid with the TiO_2 nanosheet and the RGO nanosheets closely attached among TiO_2/MoS_2 nanosheets. The 3D interconnected RGO surround around the TiO_2/MoS_2, which helps to provide strong electrical channels and conductive networks for TiO_2/MoS_2 micro-flowers, thereby ensuring the structural integrity and facilitating the effective transfer of electron during charge/discharge cycling.[24] Moreover, the permeable porous hierarchical structure can greatly reduce the transfer length for both sodium ions and electrons.[43,44]

To investigate the porous feature of the TiO_2/MoS_2/RGO hybrids, nitrogen adsorption/desorption was applied to test the structure of a series of samples. The hysteresis loops observed in Fig. 5a-c indicate the presence of abundant mesopores in the composites, which belong to typical type-Ⅲ and type-Ⅳ isotherms.[45,46] According to the isotherms, calculating shows that the TiO_2/MoS_2/RGO hybrid possesses a high BET specific surface area of 43 m^2 g^{-1}, while that of TiO_2/MoS_2 and MoS_2 possess 31.9 and 11.4 m^2 g^{-1}, respectively. The increase of specific surface area of the

TiO_2/MoS_2/RGO sample, which is attributed to the combination of RGO with MoS_2 and TiO_2, creates a number of mesoporous pores with a 3D interconnected crinkled hierarchical architecture. The pore distribution plot in Fig. 5a, b and Fig. d shows the pore size of the samples ranging from 2 to 120 nm. The large surface area, mesporous and macroporous pore size distribution of the TiO_2/MoS_2/RGO sample can not only facilitate the entry of sufficient electrolyte into internal voids within porous nanostructures of electrode, but also present plenty of electrochemical active sites and enough spaces to tackle the mechanical stress occurring in discharging/charging processes.[47]

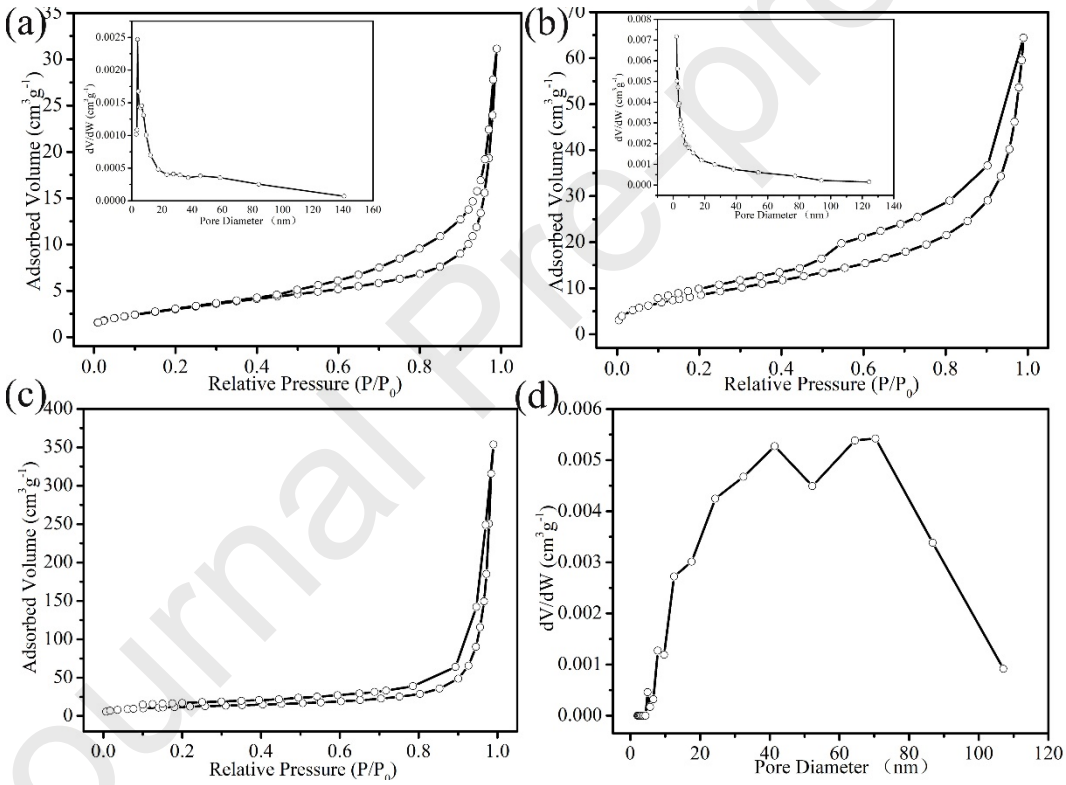

Fig. 5 Nitrogen adsorption-desorption isotherm and pore-size distribution curve: (a) MoS_2 and (b) TiO_2/MoS_2; (c) Nitrogen adsorption-desorption isotherm of TiO_2/MoS_2/RGO; (d) pore-size distribution curve of TiO_2/MoS_2/RGO.

To check metal Na^+ ions storage performance, the sample electrodes were assembled in a CR2025 coin cell with sodium metal foil as the counter electrode. With a scan rate of 0.1 mV S^{-1} and a cutoff voltage of 0.01-3.0 V, Cyclic Voltammograms (CV) curves of the first five cycles were measured to

observe the electrochemical reaction performance. As shown in Fig. 6a, the reduction peaks located at 1.3 and 0.87 V in the first cathodic process, suggesting that the Na^+ ions have inserted into TiO_2 nanosheets, the formation of solid electrolyte interphase (SEI) film and Ti^{4+} was reduced to Ti^{3+}.[48,49] According to our previous works, the peak at about 0.65 V was associated with the Na^+ diffusion into MoS_2 interlayers (forming Na_xMoS_2)[50], when it shifts to 0.15 V, Na_xMoS_2 further converted to Na_2S and metallic Mo[51]. Therefore, Fig. 6a shows that in the following anodic process, peaks at 0.65 and 0.38 V were attributed to the reconstruction of Na_xMoS_2 and the formation of MoS_2. A broad peak at a high voltage of 1.78 V, corresponding to Na_2S translated into amorphous S and the oxidation of Ti^{3+} to Ti^{4+}.[52] Contrasting to the predecessors' work about cyclic voltammograms with peak potentials of $LixTiO_2$ for TiO_2 anode materials,[34,37] the main peak voltage of TiO_2/MoS_2/RGO electrode shifted to a lower value. This phenomenon can be observed in the change range of main cathodic peak at ~ 1.0 V and anodic peak at ~ 2.2 V for convention oxide anode materials.[53] In the second cathodic curve, there are two peaks observed that are located at about 1.76 and 0.76 V, which were related to the formation of Na_2S and Mo, respectively. Compared to the first cycle, the integral area and peak intensity of CV curves present decreasing trend in the following cycles, which is caused by the SEI films arisen from the irreversible capacity of the electrode. It is noted that the CV curves for 2nd, 3rd, 4th and 5th cycle are nearly overlapped, displaying a good behavior of Na^+ ion insertion/de-intercalation reversibility of the TiO_2/MoS_2/RGO anode. We expected that each component in the electrode exhibits different roles during charging/discharging processes. The interconnected RGO layers contribute to improving electrical conductivity and mechanical stability. MoS_2 nanosheets offer more electrochemical active sites and short electron/ions transfer paths. TiO_2 nanosheets modify the MoS_2 to relieve the stress change originating from the sodium ions intercalation/de-intercalation and improve the stability of electrochemical reactions.

Fig. 6b shows the discharge-charge capacity vs potential profile for TiO_2/MoS_2/RGO electrode at the current density of 0.1 A g^{-1} for 1st, 2nd, 3th, 4th, 5th and 10th cycle. The first discharge curve appears very steep above 1.1 V, then declines to 0.8 V as the insertion of Na^+, corresponding to $TiO_2 + xNa^+ + xe^- \rightarrow NaxTiO_2$[48]. This change is agreed with the observed stage of 1.75 - 0.8 V in Fig. S5a. When the curve falls slowly to 0.56 V where sodium ions inserted into MoS_2 composition, this point can be identified by the first discharge curve of Fig. S5b. Further, the second ramp is observed up to 0.15 V, which is also accorded with the CV peak potential. However, it is distinctly different from other Mo-based compositions (such as MoO_2) with higher metal ions intercalation voltage (1.6-1.25V) under the discharge process.[36,54] The initial discharge and charge capacity deliver 1205 and 813 mA h g^{-1}, respectively, giving 67.4% for its first Coulombic efficiency. The capacity loss mainly comes from the SEI films. Discharge curves of the 2nd-10th cycles present a similar shape, and a steeper discharge plateau is observed between 1.5 V and 0.02 V, which is ascribed to the insertion to of Na^+ ions insert into the reaction sites of MoS_2[55] and TiO_2[56]. In the charge profiles, the slop line from 0.3 to 1.8 V shows the extraction of Na ions from TiO_2 and MoS_2 compounds[28,39]. Comparing to Fig. S5a and S5b, TiO_2/MoS_2/RGO electrode shows an extend insertion region for the 1st, 5th 10th cycle in Fig. 6b, which is due to its multi-composition matching effect and 3D porous interconnected architecture [57].

The cycling performance of all electrodes was evaluated at a current density of 0.1 A g^{-1} under 0.01-3.0 V. As shown in Fig. 6c, after activating at a low current density (0.05 A g^{-1}) for the first 5 cycles, the reversible capacity of the TiO_2/MoS_2/RGO electrode quickly stabilized at 610 mA h g^{-1}. As the cycling numbers increased, the capacity was pushed to 616 mA h g^{-1} after 100 cycles during the activation process. By contrast, the other samples (TiO_2/MoS_2, MoS_2, TiO_2) did not show well. In the first galvanostatic cycle, MoS_2 displays a reversible capacity of 544 mA h g^{-1} with an initial coulombic efficiency (ICE) of 79.3 %; while TiO_2 shows a reversible capacity of 253 mA h g^{-1} with

ICW of 60.1 %. From the 2nd to 5th cycle, the reversible capacity retentions of MoS_2 and TiO_2 were reduced from 98.5% to 97% and 99.9% to 99.6%, respectively. This fast capacity decay of the MoS_2 electrode originated from its block structure, resulting in pulverization of the electrode and dissolution of polysulfides. The TiO_2/MoS_2 electrode displayed a reversible capacity of 385 mA h g^{-1} after 100 cycles. The MoS_2 electrode showed a decreased capacity with cycling, reaching a reversible capacity of 141 mA h g^{-1} over 100 cycles. While the TiO_2 nanosheets electrode showed a stable cycling capacity with 225 mA h g^{-1} after 100 cycles, which was higher than that of the MoS_2 electrode.

Considering the above results, the TiO_2/MoS_2/RGO electrode showed a good cycling performance. The flexible and high conductive feature of RGO not only facilitated ion and charge transfer, but also acted as a cushion to relieve mechanical stresses of TiO_2 and MoS_2 during the discharge/charge processes.

The rate performance of the TiO_2/MoS_2/RGO, TiO_2/MoS_2 and MoS_2 samples was evaluated at current density from 0.2 A g^{-1} to 5 A g^{-1}, as shown in Fig. 6d. The TiO_2/MoS_2/RGO electrode exhibited an average capacity of 580 mA h g^{-1} at 0.2 A g^{-1} during the first 10 cycles. When the current density went up to 0.5, 1 and 2 A g^{-1}, it showed 540, 506, 410 mA h g^{-1}, respectively. With a current density of up to 5 A g^{-1}, a high capacity of 310 mA h g^{-1} can be sustained. Then, the current density went back to 0.2 A g^{-1}, the capacity reached to 670 mA h g^{-1}. As the current density increased to 5 A g^{-1}, there were only 250 and 200 mA h g^{-1} maintained for TiO_2/MoS_2 and MoS_2, respectively. TiO_2 nanosheets also showed a poor rate ability. The capacity of TiO_2/MoS_2/RGO was superior to that of TiO_2/MoS_2 and MoS_2.

The TiO_2/MoS_2/RGO sample was compared with other works in Table S2, such as MoS_2@TiO_2,[58] MoS_2@rGO,[59] MoS_2-C[60] and NiS/MoS_2/C[61]. The porous hierarchical architecture of TiO_2/MoS_2/RGO could produce more sodium storage sites, which benefited the higher initial capacity,

and reduced the barriers of Na^+ mobility, contributing to an excellent electrochemical performance.[62]

The electrochemical impedance spectroscopy (EIS) analysis suggested that the TiO_2/MoS_2/RGO electrode possesses a good charge transfer kinetics. Fig. S5 shows that EIS data of TiO_2, MoS_2, TiO_2/MoS_2 and TiO_2/MoS_2/RGO with metal Li as the counter electrode at the open voltage (2.2 V to 3.0 V), the frequency range of 10 MHz to 100 kHz. Re represents the resistance of the electrolyte, electrode and separator in the high-frequency region; the semicircle stands for charge transfer resistance (Rct) in the medium-frequency region, and the slant line represents the Warburg impedance (Zw) in the low-frequency region. Compared with TiO_2/MoS_2, MoS_2 and TiO_2, TiO_2/MoS_2/RGO electrode had a low charge-transfer resistance (Rct) of 133 Ω in the equivalent circuit. Corresponding Rct values of TiO_2/MoS_2, MoS_2 and TiO_2 electrodes were about 225, 230 and 376 Ω, respectively. Synergetic effect of the three components and the interconnected porous architecture prompted Rct of TiO_2/MoS_2/RGO electrode to a relatively small value.[63]

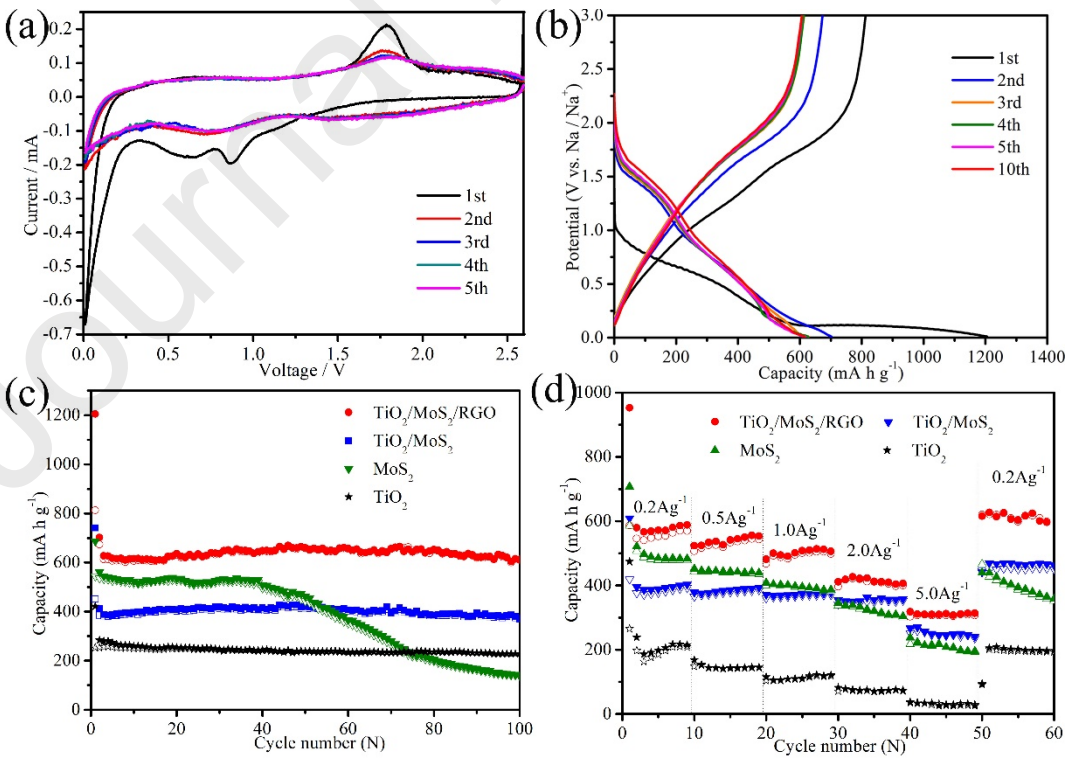

Fig. 6 The electrochemical performance of the samples. (a) CV curves for TiO_2/MoS_2/RGO anode on the five cycles

operated at a scan rate of 0.1 mV s^{-1} and voltage range of 3.0-0.01 V; (b) Discharge-charge property of the TiO_2/MoS_2/RGO at a current density of 0.1 A g^{-1} in the voltage range 3.0-0.01 V; (c) Cycling performance of TiO_2, MoS_2, TiO_2/MoS_2 and TiO_2/MoS_2/RGO hybrid electrodes anode at 0.1 A g^{-1}; (d) Rate capabilities of TiO_2, MoS_2, TiO_2/MoS_2 and TiO_2/MoS_2/RGO hybrid electrodes.

To further explore the stability performance of the TiO_2/MoS_2/RGO electrode with a porous hierarchical structure, the current density of the cycling test was set to 1 A g^{-1}. In the first four cycles, low current density values of 0.05, 0.1, 0.2, and 0.5 A g^{-1} were conducted to activate the electrode. As shown in Fig. 7a, after 350 cycles, the TiO_2/MoS_2/RGO electrode maintained a discharge capacity of 460 mA h g^{-1}. Furthermore, in the first 25 cycles, the coulombic efficiency increased and was then kept at around 100%. A superior storage of Na^+ ions of the TiO_2/MoS_2/RGO electrode indicated synergistic effects among the MoS_2 layers, TiO_2 nanosheets and RGO. During the Na^+ ions inserion/de-intercalation process, TiO_2 nanosheets presented their stable nature, showing the passivation and buffer feature to prevent the corrosion and collapse of MoS_2.[64] The interconnected RGO layers among TiO_2/MoS_2 nanosheets relaxed electrochemical redox strains and lowered barriers of MoS_2 for Na^+ insertion/de-insertion.[65] Fig. 7b indicates the EIS spectra of the TiO_2/MoS_2/RGO fresh electrode and cycling for 50, 350 cycles. In the fitted equivalent circuit, Rsf refers to the SEI surface film resistance of the electrode. The fitted value of Rct for the fresh electrode is 133 Ω. After 50 cycles and 350 cycles, in the fully charged-state at 2.6 V, the corresponding R(sf+ct) values reduced from 120 Ω to 52 Ω. It is found that the surface film resistance and the multi-component electrode with porous hierarchical architecture facilitate the kinetics of insertion/desertion of Na ions with increasing the cycle numbers. As discussed by M. V. Reddy[66,67], the systematic resistance decreases from the fresh electrode, 50 cycles to 350 cycles, which was because the surface film resistance possibly became negligibly small after 350 cycles.

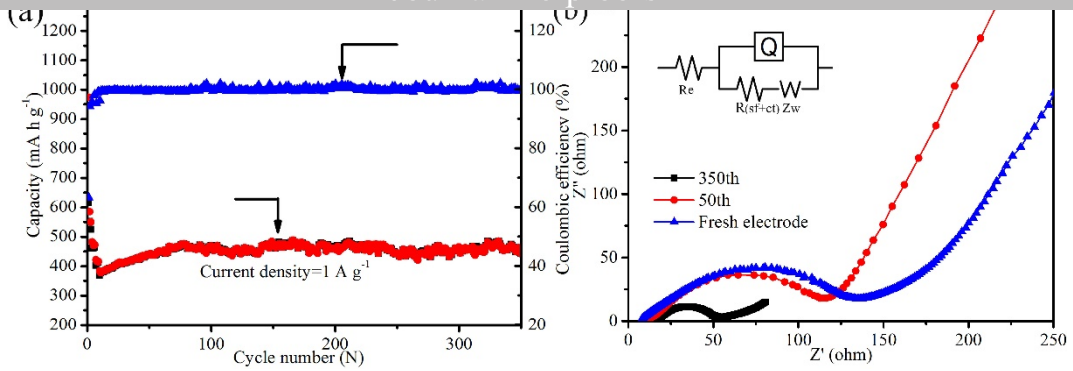

Fig. 7 (a) the long cycling performance at current density of 1 A g^{-1} and (b) EIS spectrum of the of TiO_2/MoS_2/RGO hybrid electrode.

Moreover, to validate the porous hierarchical architecture stability of active materials during discharge/charge processes, we disassembled the coin cell after 350 cycles. After washing and drying, from the SEM images (Fig. 8), the microstructural shape of the TiO_2/MoS_2/RGO sample maintained its original hierarchical nanostructure, without any collapse and shedding. This indicates that the porous hierarchical architecture plays a crucial role in maintaining structural integrity of active materials under the repeated Na^+ insertion/de-intercalation processes. Additionally, the multi - component matching effect enhanced the cycling stability of electrode. The MoS_2 was modified by TiO_2 nanosheets to relieve the stress changes derived from sodium ion intercalation/de-intercalation. Following the introduction of RGO, the charge-transfer resistance of TiO_2/MoS_2 was reduced by the interconnected architecture. A 3D porous hierarchical architecture with abundant pores provided unblocked channels for electrolytes and shortened the distance of electron and ion transport, resulting in a good structure for Na^+ storage.[68]

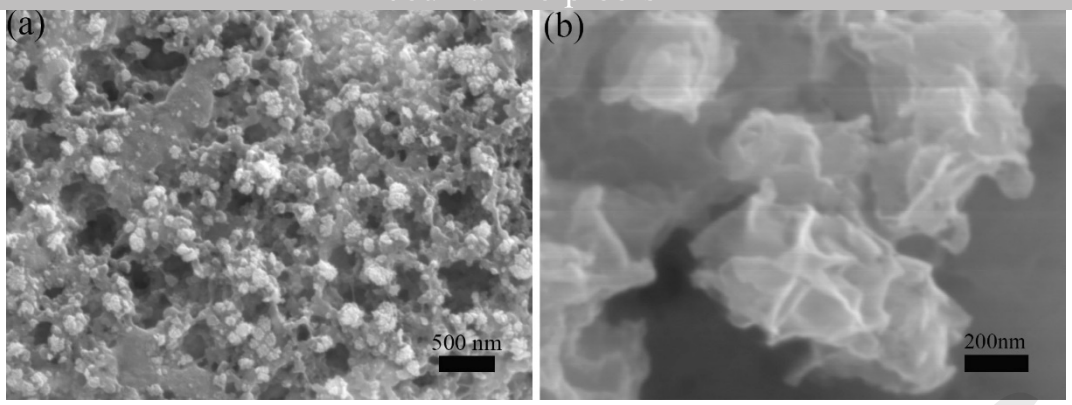

Fig. 8 SEM images (a, b) of the TiO_2/MoS_2/rGO hybrid electrode for SIBs at a potential of 3.0 V after 350 cycles.

4. Conclusions

Above all, a porous hierarchical TiO_2/MoS_2/RGO architecture was synthesized by hydrothermal and calcination method. We explored the synergistic effects among TiO_2 nanosheets, MoS_2 multilayer structure and the linked RGO to improve the Na-storage performance of the TiO_2/MoS_2/RGO anode material for SIBs. Compared with TiO_2/MoS_2 and MoS_2, the TiO_2/MoS_2/RGO sample delivered a reversible capacity of 616 mA h g^{-1} at 0.1 A g^{-1} and maintained at 460 mA h g^{-1} for 350 cycles at a high current density of 1 A g^{-1}, accompanied by an outstanding rate performance capability (615 mA h g^{-1} at 0.2 A g^{-1}; 250 mA h g^{-1} at 5A g^{-1}). This study suggests that a porous hierarchical architecture with a synergistic effect among different nanosized components is an effective strategy to enhance its electrochemical performances when the electrode is applied to sodium ion batteries.

Acknowledgements

This work was supported by the National Youth Science Foundation of China (No.: 51702177), the National Nature Science Foundation of China (No.: 51472148) and the Tai Shan Scholar Foundation of Shandong Province.

References

[1] M. V. Reddy, G. V. Subba Rao, B. V. R. Chowdari, Metal oxides and oxysalts as anode materials for Li ion batteries. *Chem. Rev*., 2013, **113**, 5364-5457.

[2] M. V. Reddy, A. Mauger, C. M. Julien, A. Paolella, K. Zaghib, Brief History of Early Lithium-Battery Development. *Materials*, 2020, **13**, 1884.

[3] JY. Hwang, ST. Myung, YK. Sun, Sodium-ion batteries: present and future, *Chem. Soc. Rev.,* 2017, **46**, 3529-3614.

[4] Y. Liang, WH. Lai, Z. Miao, SL. Chou, Nanocomposite materials for the sodium-ion battery, *Small*, 2018, **14**, 1702514.

[5] F. Wu, C. Zhao, S. Chen, Y. Lu, Y. Hou, Y-S. Hu, J. Maier, Y. Hu. Multi-electron reaction materials for sodium-based batteries. *Materials Today*, 2018, **21**, 960-973.

[6] X. Hu, W. Zhang, X. Liu, Y. Mei, Y. Huang, Nanostructured Mo-based electrode materials for electrochemical energy storage, *Chem. Soc. Rev.,* 2015, **44**, 2376-2404.

[7] Z. Li, Z. Jian, X. Wang, IA. RodríguezPérez, C. Bommier, X. Ji, Hard carbon anodes of sodium-ion batteries: undervalued rate capability, *Chem. Commun.,* 2017, **53**, 2610-2613.

[8] N. Ingersoll, Z. Karimi, D. Patel, R. Underwood, R. Warren, Metal organic framework-derived carbon structures for sodium-ion battery anodes, *Electrochim Acta,* 2019, **297**, 129-136.

[9] J. Ye, J. Zang, Z. Tian, M. Zheng, Q. Dong, Sulfur and nitrogen co-doped hollow carbon spheres for sodium-ion batteries with superior cyclic and rate performance, *J. Mater. Chem. A,* 2016, **4**, 13223-13227.

[10] X. Ma, X. Xiong, J. Zeng, P. Zou, Z. Lin, M. Liu. Melamine-assisted synthesis of Fe_3N featuring highly reversible crystalline-phase transformation for ultrastable sodium ion storage. *J. Mater. Chem. A*, 2020, **8**, 6768-6775.

[11] F. Xie, L. Zhang, D. Su, M. Jaroniec, SZ. Qiao, $Na_2Ti_3O_7$@ N-Doped Carbon Hollow Spheres for Sodium-Ion Batteries with Excellent Rate Performance, *Adv. Mater.,* 2017, **29**, 1700989.

[12] Z. Hu, Q. Liu, SL. Chou, SX. Dou, Advances and challenges in metal sulfides/selenides for next-generation rechargeable sodium-ion batteries, *Adv. Mater.,* 2017, **29**, 1700606.

[13] Z. Liu, T. Lu, T. Song, XY. Yu, XW. Lou, U. Paik, Structure-designed synthesis of FeS_2@C yolk-shell nanoboxes as a high-performance anode for sodium-ion batteries, *Energy Environ. Sci.,* 2017, **10**, 1576-1580.

[14] D.Yang, B. Xu, Q. Zhao, XS. Zhao, Three-dimensional nitrogen-doped holey graphene and transition metal oxide composites for sodium-ion batteries, *J. Mater. Chem. A,* 2019, **7**, 363-371.

[15] PR. Abel, MG. Fields, A. Heller, C.B. Mullins, Tin-Germanium alloys as anode materials for sodium-ion batteries, *ACS Appl. Mater. Interfaces,*2014, **6**, 15860-15867.

[16] Z. Liu, XY. Yu, X. W. Lou, U. Paik, Sb@C coaxial nanotubes as a superior long-life and high-rate anode for sodium ion batteries, *Energy Environ. Sci.,* 2016, **16**, 2314-2318.

[17] C. Zhao, X. Wang, J. Kong, JM. Ang, PS. Lee, Z. Liu, X. Lu, Self-assembly-induced alternately stacked single-layer MoS_2 and N-doped graphene: A novel van der Waals heterostructure for lithium-ion batteries, *ACS Appl. Mater. Interfaces,* 2016, **8**, 2372-2379.

[18] D. Su, S. Dou, G. Wang, Ultrathin MoS_2 nanosheets as anode materials for sodium-ion batteries with superior performance, *Adv. Ener. Mat.,* 2015, **5**, 1401205.

[19] SK. Park, J. Lee, S. Bong, B. Jang, KD. Seong, Y. Piao, Scalable synthesis of few-layer MoS_2 incorporated into hierarchical porous carbon nanosheets for high-performance Li-and Na-ion battery anodes, *ACS Appl. Mater. Interfaces*, 2016, **8**, 19456-19465.

[20] X. Xie, Z. Ao, D. Su, J. Zhang, G. Wang, MoS_2/Graphene Composite Anodes with Enhanced Performance for Sodium-Ion Batteries: The Role of the Two-Dimensional Heterointerface, *Adv. Func.*

Mat., 2015, **25**, 1393-1403.

[21] X. Li, W. Li, M. Li, P. Cui, D. Chen, T. Gengenbach, L. Chu, H. Liu, G. Song, Glucose-assisted synthesis of the hierarchical TiO_2 nanowire@ MoS_2 nanosheet nanocomposite and its synergistic lithium storage performance, *J. Mater. Chem. A,* 2015, **3**, 2762-2769.

[22] R. Dai, A. Zhang, Z. Pan, AM. Al-Enizi, AA. Elzatahry, L. Hu, G. Zheng, Epitaxial Growth of Lattice-Mismatched Core-Shell TiO_2@ MoS_2 for Enhanced Lithium-Ion Storage, *Small*, 2016, **12**, 2792-2799.

[23] YL. Bai, XY. Wu, YS. Liu, C. Ma, X. Wei, KX. Wang, JS. Chen, Dandelion-clock-inspired preparation of core-shell TiO_2@ MoS_2 composites for high performance sodium ion storage, *J. Alloy. Compd,* 2020, **815**, 152386.

[24] S. Anwer, Y. Huang, B. Li, B. Govindan, K. Liao, WJ. Cantwell, F. Wu, R. Chen, L. Zheng, Nature-inspired, graphene-wrapped 3D MoS_2 ultrathin microflower architecture as a high-performance anode material for sodium-ion batteries, *ACS Appl. Mater. Interfaces*, 2019, **11**, 22323-22331.

[25] Y. Teng, H. Zhao, Z. Zhang, L. Zhao, Y. Zhang, Z. Li, Q. Xia, Z. Du, K. Świerczek. MoS_2 nanosheets vertically grown on reduced graphene oxide via oxygen bonds with carbon coating as ultrafast sodium ion batteries anodes. Carbon, 2017, 119, 91-100.

[26] J. Yu, J. Fan, K. Lv, Anatase TiO_2 nanosheets with exposed (001) facets: improved photoelectric conversion efficiency in dye-sensitized solar cells, *Nanoscale*, 2010, **2**, 2144-2149.

[27] J. Chen, F. Chi, L. Huang, M. Zhang, B. Yao, Y. Li, C. Li, G. Shi. Synthesis of graphene oxide sheets with controlled sizes from sieved graphite flakes. *Carbon*, 2016, **110**, 34-40.

[28] Y. Wu, X. Liu, Z. Yang, L. Gu, Y. Yu, Nitrogen-Doped Ordered Mesoporous Anatase TiO_2 Nanofibers as Anode Materials for High Performance Sodium-Ion Batteries, *Small*, 2016, **12**, 3522-

3529.

[29] K. Chang, D. Geng, X. Li, J. Yang, Y. Tang, M. Cai, R. Li and X. Sun, Ultrathin MoS_2/Nitrogen-Doped Graphene Nanosheets with Highly Reversible Lithium Storage, *Adv. Energy Mater*., 2013, **3**, 839-844.

[30] M. Naebe, J. Wang, A. Amini, H. Khayyam, N. Hameed, LH. Li, Y. Chen, B. Fox, Mechanical property and structure of covalent functionalised graphene/epoxy nanocomposites, *Sci. rep*., 2014, **4**, 4375.

[31] Y. Gong, S. Yang, L. Zhan, L. Ma, R. Vajtai, PM. Ajayan, A Bottom-Up Approach to Build 3D Architectures from Nanosheets for Superior Lithium Storage, *Adv. Funct. Mater*., 2014, **24**, 125-130.

[32] M. V. Reddy, S. Aadams, G. T. J. Liang, I. F. Mingze, H. V.T. An, B. V. R. Chowdari. Low temperature molten salt synthesis of anatase TiO_2 and its electrochemical properties. Solid State Ionics, 2014, **262**, 120-123.

[33] P. Zhu, Y. Wu, M. V. Reddy, A. S. Nair, B. V. R. Chowdari and R. Ramakrishna. Long term cycling studies of electrospun TiO_2 nanostructures and their composites with MWCNTs for rechargeable Li-ion batteries. 2012, **2**, 531-537.

[34] C. T. Cherian, M. V. Reddy, T. Magdaleno, C-H, Sow, K. V. Ramanujachary, G. V. Subba and B. V. R. Chowdari. (N, F)-Co-doped TiO_2: synthesis, anatase-rutile conversion and Li-cycling properties. CrystEngComm, 2012, **14**, 978-986.

[35] X. He, L. Bi, Y. Li, C. Xu, D. Lin, CoS_2 embedded graphitic structured N-doped carbon spheres interlinked by rGO as anode materials for high-performance sodium-ion batteries, *Electrochimica Acta*, 2020, **332**, 135453.

[36] M. V. Reddy, N. Sharma, S. Adams, R. P. Rao, V. K. Peterson and B. V. R. Chowdari. Evaluation of undoped and M-doped TiO_2, where M= Sn, Fe, Ni/Nb, Zr, V, and Mn, for lithium-ion battery

applications prepared by the molten-salt method. *RSC Adv.*, 2015, **5**, 29535-29544.

[37] M. Mao, L. Mei, D. Guo, L. Wu, D. Zhang, Q. Li and T. Wang, High electrochemical performance based on the TiO_2 nanobelt@ few-layered MoS_2 structure for lithium-ion batteries, *Nanoscale*, 2014, **6**, 12350-12353.

[38] S. Petnikota, K. W. Teo, L. Chen, A. Sim, S. K. Marka, M. V. Reddy, V. V. S. S. Srikanth, S. Adams and B. V. R. Chowdari. Exfoliated Graphene Oxide/MoS_2 Composites as Anode Materials in Lithium-Ion Batteries: An Insight Into Intercalation of Li and Conversion Mechanism of MoO_2, *ACS Appl. Mater. Interfaces*, 2016, **8**, 17, 10884-10896.

[39] D. Xie, X. Xia, Y. Wang, D. Wang, Y. Zhong W. Tang, X. Wang, J. Tu, Nitrogen-Doped Carbon Embedded MoS_2 Microspheres as Advanced Anodes for Lithium-and Sodium-Ion Batteries, *Chem. - A Eur. J.*, 2016, **22**, 11617-11623.

[40] J. Xu, M. Wang, NP. Wickramaratne, M. Jaroniec, S. Dou, L. Dai, High-performance sodium ion batteries based on a 3D anode from nitrogen-doped graphene foams, *Adv. Mater.*, 2015, **27**, 2042-2048.

[41] N. Li, G. Liu, C. Zhen, F. Li, L. Zhang, HM. Cheng, Battery performance and photocatalytic activity of mesoporous anatase TiO_2 nanospheres/graphene composites by template-free self-assembly, *Adv. Funct. Mater.*, 2011, **21**, 1717-1722.

[42] X. Yin, Y. Yan, M. Miao, K. Zhan, P. Li, J. Yang, B. Zhao, BY. Xia, Quasi-Emulsion Confined Synthesis of Edge-Rich Ultrathin MoS_2 Nanosheets/Graphene Hybrid for Enhanced Hydrogen Evolution, *Chem. - A Eur. J.*, 2018, **24**, 556-560.

[43] S. Wang, BY. Guan, L. Yu, XW. Lou, Rational design of three-layered TiO_2@ Carbon@ MoS_2 hierarchical nanotubes for enhanced lithium storage, *Adv. Mater.*, 2017, **29**, 1702724.

[44] S. Wang, Y. Fang, X. Wang, XW. Lou, Hierarchical Microboxes Constructed by SnS Nanoplates

Coated with Nitrogen-Doped Carbon for Efficient Sodium Storage, *Angew. Chem. Int. Ed.*, 2019, **58**, 760-763.

[45] M. Wang, H. Fei, P. Zhang, L. Yin, Hierarchically layered MoS_2/Mn_3O_4 hybrid architectures for electrochemical supercapacitors with enhanced performance, *Electrochimica Acta*, 2016, **209**, 389-398.

[46] R. Tian, W. Wang, Y. Huang, H. Duan, Y. Guo, H. Kang, H. Li, H. Liu, 3D composites of layered MoS_2 and graphene nanoribbons for high performance lithium-ion battery anodes, *J. Mater. Chem. A*, 2016, **4**, 13148-13154.

[47] W. Ye, L. Yu, M. Sun, G. Cheng, S. Fu, S. Peng, S. Han, X. Yang, Yolk-shell Prussian blue analogues hierarchical microboxes: Controllably exposing active sites toward enhanced cathode performance for lithium ion batteries, *Electrochimica Acta*, 2019, **319**, 237-244.

[48] Y. Yang, S. Wang, S. Lin, Y. Li, W. Zhang, Y. Chao, M. Luo, Y. Xing, K. Wang, C. Yang, P. Zhou, Y. Zhang, Z. Tang, S. Guo, Rational Design of Hierarchical TiO_2/Epitaxially Aligned MoS_2-Carbon Coupled Interface Nanosheets Core/Shell Architecture for Ultrastable Sodium-Ion and Lithium-Sulfur Batteries, *Small Methods*, 2018, **2**, 1800119.

[49] KT. Kim, G. Ali, KY. Chung, CS. Yoon, H. Yashiro, YK. Sun, J. Lu, K. Amine, ST. Myung, Anatase titania nanorods as an intercalation anode material for rechargeable sodium batteries, *Nano Letters*, 2014, **14**, 416-422.

[50] S. Liu, Y. Yin, M. Wu, KS. Hui, KN. Hui, CY. Ouyang, SC. Jun, Phosphorus-Mediated MoS_2 Nanowires as a High-Performance Electrode Material for Quasi-Solid-State Sodium-Ion Intercalation Supercapacitors, *Small*, 2019, **15**, 1803984.

[51] W. Ren, H. Zhang, C. Guan, C. Cheng, Ultrathin MoS_2 nanosheets@ metal organic framework-derived N-doped carbon nanowall arrays as sodium ion battery anode with superior

cycling life and rate capability, *Adv. Funct. Mater*., 2017, **27**, 1702116.

[52] W. Zhuang, L. Li, J. Zhu, R. An, L. Lu, X. Lu, X. Wu, H. Ying, Facile synthesis of mesoporous MoS_2-TiO_2 nanofibers for ultrastable lithium ion battery anodes, *ChemElectroChem*, 2015, **2**, 374-381.

[53] M. V. Reddy, X. V. Teoh, T. B. Nguyen, Y. M. Lim, B. V. R. Chowdari, Effect of 0.5 M $NaNO_3$: 0.5 M KNO_3 and 0.88 M $LiNO_3$: 0.12 M LiCl molten salts, and heat treatment on electrochemical properties of TiO_2. J. Electrochem. Soc., 2012, **159**, A762.

[54] M. Chen, X. Yin, M. V. Reddy and S. Adams. All-solid-state MoS_2/Li_6PS_5Br/In-Li batteries as a novel type of Li/S battery. *J. Mater. Chemis. A*, 2015, **3**, 10698-10702.

[55] X. Xiong, W. Luo, X. Hu, C. Chen, L. Qie, D. Hou, Y. Huang, Flexible membranes of MoS_2/C nanofibers by electrospinning as binder-free anodes for high-performance sodium-ion batteries, *Sci. rep*., 2015, **5**, 9254.

[56] S. Qiu, L. Xiao, X. Ai, H. Yang, Y. Cao, Yolk-shell TiO_2@ C nanocomposite as high-performance anode material for sodium-ion batteries, *ACS Appl. Mater. Interfaces*, 2017, **9**, 345-353.

[57] M. Vellaisamy, M. V. Reddy, B. V. R. Chowdari and N. Kalaiselvi. Exploration of AVP_2O_7/C (A=Li, $Li_{0.5}Na_{0.5}$, and Na) for High-Rate Sodium-Ion Battery Applications. *J. Phys. Chem. C*, 2018, **122**, 43, 24609-24618.

[58] YL. Bai, XY. Wu, YS. Liu, C. Ma, X. Wei, KX. Wang, JS. Chen, Dandelion-clock-inspired preparation of core-shell TiO_2@ MoS_2 composites for high performance sodium ion storage, *J. Alloy. Compd*., 2020, **815**, 152386.

[59] Z. Che, Y. Li, K. Chen, M. Wei, Hierarchical MoS_2@ RGO nanosheets for high performance sodium storage, *J. Power Sources*, 2016, **331**, 50-57.

[60] L. Liu, R. Shi, Y. Li, Y. Wu, K. Ye, X. Yan, Y. Shi, C. Cao, In Situ Constructing MoS_2-C

Nanospheres as Advanced Anode for Sodium-Ion Battery, *ChemistrySelect*, 2018, **3**, 11381-11387.

[61] H. Xie, M. Chen, L. Wu, Hierarchical Nanostructured NiS/MoS_2/C Composite Hollow Spheres for High Performance Sodium-Ion Storage Performance, *ACS Appl. Mater. Interfaces*, 2019, **11**, 41222-41228.

[62] H. Hou, C. E. Banks, M. Jing, Y. Zhang, X. Ji. Carbon Quantum Dots and Their Derivative 3D Porous Carbon Frameworks for Sodium-Ion Batteries with Ultralong Cycle Life. *Adv. Mater*., **2015**, 27, 7861-7866

[63] X. Ma, X. Xiong, P. Zou, W. Liu, F. Wang, L. Liang, Y. Liu, C. Yuan, Z. Lin. General and Scalable Fabrication of Core-Shell Metal Sulfides@ C Anchored on 3D N-Doped Foam toward Flexible Sodium Ion Batteries. *Small*, **2019**, 15(45), 1903259.

[64] N. Wang, J. Yue, L. Chen, Y. Qian, J. Yang, Hydrogenated TiO_2 branches coated Mn_3O_4 nanorods as an advanced anode material for lithium ion batteries, *ACS Appl. Mater. Interfaces*, 2015, **7**, 10348-10355.

[65] SH. Choi, YN. Ko, JK. Lee, YC. Kang, 3D MoS_2-graphene microspheres consisting of multiple nanospheres with superior sodium ion storage properties, *Adv. Funct. Mater*., 2015, **25**, 1780-1788.

[66] M. V. Reddy, B. L. Wei Wen, K. P. Loh, B. V. R. Chowdari, Energy storage studies on $InVO_4$ as high performance anode material for Li-ion batteries. *ACS Appl. Mater. Interfaces*, 2013, 5(16), 7777-7785.

[67] M. V. Reddy, G. S. Rao, B. V. R. Chowdari, Nano-($V_{1/2}$ $Sb_{1/2}$ Sn) O_4: a high capacity, high rate anode material for Li-ion batteries. *J. Mater. Chem*. **2011**, 21(27), 10003-10011.

[68] D. Zhao, R. Zhao, S. Dong, X. Miao, Z. Zhang, C. Wang, L. Yin, Alkali-induced 3D crinkled porous Ti_3C_2 MXene architectures coupled with NiCoP bimetallic phosphide nanoparticles as anodes for high-performance sodium-ion batteries, *Energy Environ. Sci*., 2019, **12**, 2422-32.

Highlight

1. TiO_2 nanosheets and RGO layers modify MoS_2 layers to realize porous hierarchical TiO_2/MoS_2/RGO architecture;
2. The unique porous hierarchical nanostructure provided unblocked channels for electrolyte and shortened the distance of electron and ion transport when it applied as anode material for SIBs;
3. The synergistic effect amongTiO_2, MoS_2 and RGO with 3D interconnected network improved the electrochemical performance.

Graphical abstract

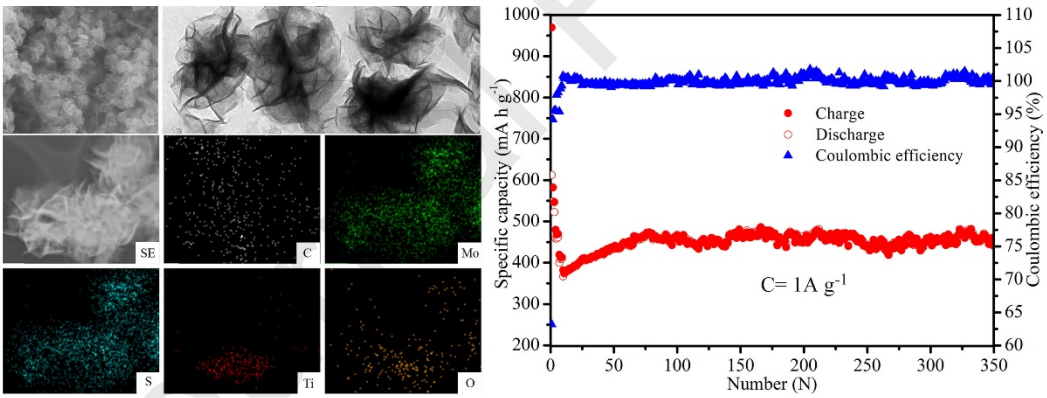

Declaration of interests

☐ √ The authors declare that they have no known competing financial interests or personal relationships that could have appeared to influence the work reported in this paper.

☐The authors declare the following financial interests/personal relationships which may be considered as potential competing interests:

Jingyun Ma
Mengdi Xing
Longwei Yin
Kwan San Hui
Kwun Nam Hui

Credit author statement

According to the work of "Porous Hierarchical TiO_2/MoS_2/RGO nanoflowers as Anode Material for Sodium Ion Batteries with High Capacity and Stability", the contribution of this paper is shown as below:

Jingyun Ma: designing the schedule of the work, investigation, performing sample preparation, characterization, performance testing, writing - reviewing and editing, project administration and acquisition of the financial support for the project leading to this work completing;

Mengdi Xing: performing sample preparation and performance testing; writing - original draft;

Longwei Yin: supervision; acquisition of the financial support for the project leading to this work completing;

Kwan San Hui: writing - reviewing and editing; investigation;

Kwun Nam Hui: editing.

Signature: Jingyun Ma